Edge-coherent-mode nature of the small edge localized modes in Experimental Advanced Superconducting Tokamak

H. Q. Wang, G. S. Xu, H. Y. Guo, B. N. Wan, L. Wang, R. Chen, S. Y. Ding, N. Yan, X. Z. Gong, S. C. Liu, L. M. Shao, L. Chen, W. Zhang, Y. F. Liang, G. H. Hu, Y. L. Liu, Y. L. Li, and N. Zhao

Edge-coherent-mode nature of the small edge localized modes in Experimental Advanced Superconducting Tokamak

H. Q. Wang,[1] G. S. Xu,[1] H. Y. Guo,[1,2] B. N. Wan,[1] L. Wang,[1] R. Chen,[1] S. Y. Ding,[1] N. Yan,[1] X. Z. Gong,[1] S. C. Liu,[1] L. M. Shao,[1] L. Chen,[1] W. Zhang,[1] Y. F. Liang,[1,3] G. H. Hu,[1] Y. L. Liu,[1] Y. L. Li,[1] and N. Zhao[1]

[1]*Institute of Plasma Physics, Chinese Academy of Sciences, Hefei 230031, China*
[2]*General Atomics, P.O. Box 85608, San Diego, California 92186-5608, USA*
[3]*Forschungszentrum Jülich GmbH, Association EURATOM-FZ Jülich, Institut für Energie und Klimaforschung Plasmaphysik, Trilateral Euregio Cluster, D-52425 Jülich, Germany*

(Received 17 June 2014; accepted 4 September 2014; published online 23 September 2014)

High-confinement regime with high-frequency and low-energy-loss small edge localized modes (ELMs) was achieved in Experimental Advanced Superconducting Tokamak by using the lower hybrid current drive and ion cyclotron resonance heating with lithium wall conditioning. The small ELMs are usually accompanied with a quasi-coherent mode at frequency around 30 kHz, as detected by the Langmuir probes near the separatrix. The coherent mode, with weak magnetic perturbations different from the precursor of conventional ELMs, propagates in the electron diamagnetic drift direction in the lab frame with the poloidal wavelength $\lambda_\theta \sim 14 \, \text{cm}$, corresponding to both high poloidal and toroidal mode numbers (m > 60 and n > 12). This coherent mode, carrying high-temperature high-density filament-like plasma, drives considerable transport from the pedestal region into the scrape-off layer towards divertor region. The co-existence of small ELMs and quasi-coherent modes is beneficial for the sustainment of long pulse H-mode regime without significant confinement degradation. © 2014 AIP Publishing LLC. [http://dx.doi.org/10.1063/1.4896237]

I. INTRODUCTION

Understanding the dynamics of the edge localized modes (ELMs) has attracted broad interest in the magnetic confinement fusion, since the high confinement regime known as H-mode was found more than 30 years ago.[1] H-mode, characterized by the presence of an edge transport barrier or pedestal, is a promising operational regime for a magnetic confinement fusion device due to its superior energy confinement. During the formation of the pedestal, the increase of plasma density and temperature gradients on the one hand leads to a substantial gain in energy and fusion performance, but on the other hand, reaches a critical limit above which edge instabilities become unstable.[2,3] ELMs, as the most common MHD instabilities, lead to the cyclic relaxation of the transport barrier and result in transport out from core plasma, which are thought to be beneficial for the sustainment of high-performance plasma.[4–6] However, giant ELMs or type-I ELMs may cause serious damage to plasma-facing components and impose operational constraints in ITER and future reactors.[7] Therefore, small ELMs or other pedestal/edge instabilities, which are able to result in benign and considerable particle and impurity transport, and accompanied with high energy confinement have attracted broad interest.[8–15]

Such a kind of small ELMy regime with energy confinement factor $H_{98y,2}$ up to 1 has been achieved in Experimental Advanced Superconducting Tokamak (EAST) by RF-heating and lithium wall conditioning. The small ELMs lead to much smaller heat load on the divertor target plate with higher frequency than type-III ELMs. An edge quasi-coherent mode (ECM) with frequency around 30 kHz has been directly detected by the edge Langmuir probes near the low-field-side midplane. The ECM-induced filament structures, with high temperature and density fluctuations (4 times of the ELM-free plasma), have been found to be responsible for the ELMs transport toward the divertor region. This evidence of the coherent-mode structure, different from the type-I or type-III ELMs but similar to that of type-II ELMs,[15,16] may have some implications for understanding of the small ELMs.

In this paper, we first give a brief introduction of the small ELMy H-mode in Sec. II and then describe some characteristics of the small ELMs in Sec. III. The detailed dynamic structure of the small ELMs is presented in Sec. IV, with the direct measurement of the edge coherent mode. Finally, a brief summary is given in Sec. V.

II. SMALL ELMy H-MODES

The small ELMy H-modes have been obtained in EAST in 2012 experimental campaign. EAST is a medium-sized tokamak with major radius $R_0 = 1.88 \, \text{m}$, minor radius $a = 0.45 \, \text{m}$, toroidal magnetic field $B_T < 3 \, \text{T}$, plasma current $I_p < 1 \, \text{MA}$, elongation ratio $\kappa = 1.2$–2, and triangularity $\delta \leq 0.8$.[17] H-modes, with the normalized electron collisionality at the pedestal top $\nu_e^* > 1$,[18] are usually obtained with a combination of lower hybrid current drive (LHCD) and ion cyclotron resonance heating (ICRH) accompanying with lithium wall conditioning.[19] Both LHCD and ICRF (ion cyclotron range of frequency) heating do not provide direct momentum injection, in contrast to the Neutral Beam Injection (NBI), which is the main heating source for the achievement of the type-II ELMy H-mode in ASDEX-Upgrade.[16]
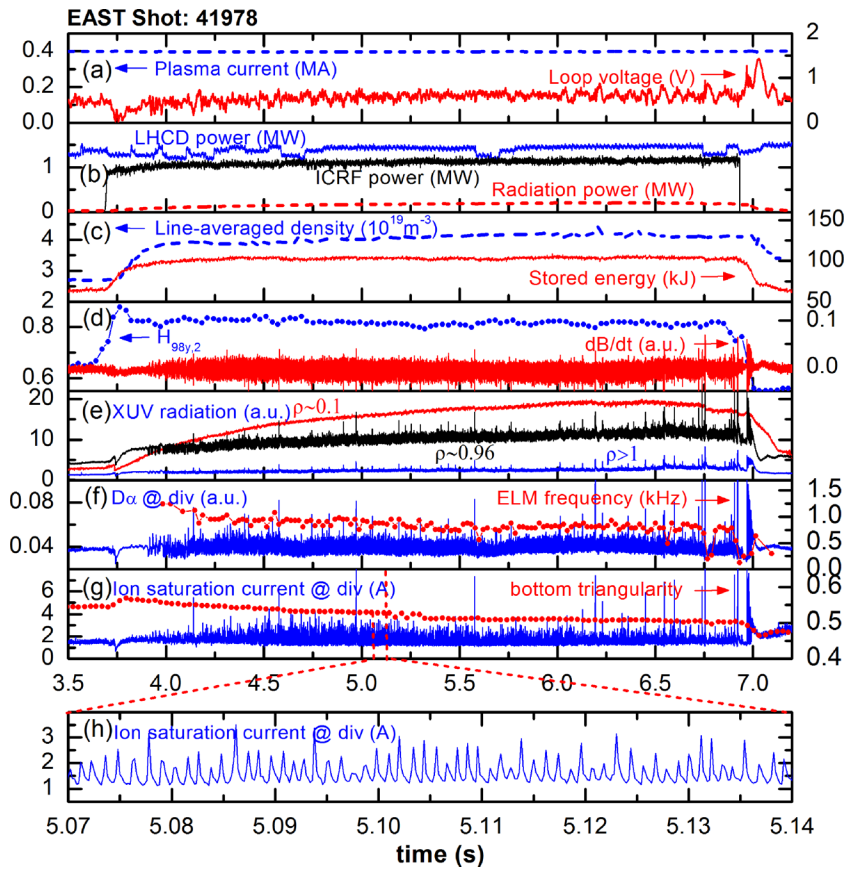
FIG. 1. Time evolution of a typical small-ELM H-mode discharge: (a) plasma current I_p (dashed line), loop voltage (red solid); (b) injecting LHCD power (blue line), ICRF source heating power (black line), and radiation power; (c) central-line-averaged density (blue dashed line) and stored energy W_{dia} (red solid line); (d) energy confinement factor $H_{98y,2}$ (blue dotted line) and magnetic perturbation (red line) measured by the Mirnov coils installed at the midplane of high-field side; (e) XUV radiations at core region, near pedestal region and divertor region; (f) divertor D_α emission (blue line), ELMs repetition frequency (red circle); (g) divertor ion saturation current measured by Langmuir probe (blue line), bottom triangularity (red circle); (h) zoom-in plot of the ion saturation current between 5.07 s and 5.14 s. The L-H transition occurs at $\sim$3.75 s, while the H-L transition $\sim$7 s.

Figure 1 shows a typical lower-single null ($dR_{sep} \sim -1.2$ cm) small-ELMy H-mode discharge with normalized density $n_e/n_G \sim 0.58$ ($n_G \sim I_p/(\pi a^2)$), elongation $\kappa \sim 1.7$, and edge safety factor $q_{95} \sim 5$. The power through the separatrix, which includes 1.2 MW injected LHCD power and $\sim$1 MW ICRF source power, is estimated to be $\sim$1.4 times the L-H transition threshold power. The small ELMs, accompanying with sporadic type-III ELMs, appear at $\sim$150 ms after L-H transition and last for about 3 s ($\sim$50 times the energy confinement time), which is limited by the duration of heating. In this discharge, the small-ELM regime is changed to type-III ELMy phase after the termination of the ICRH. The ELMs repetition frequency decreases from 1.2 kHz at the onset to 0.8 kHz (Fig. 1(f)), while at the same time the bottom triangularity decrease from 0.6 to 0.5.

During the whole small ELMy regime, the line-averaged density and plasma stored energy (Fig. 1(c)) are nearly constant, presumably because that the small ELMs provide intermittent particle and power exhaust, which is beneficial for the sustainment of H-mode, allowing good maintenance of plasma density for long pulse operations. Furthermore, from the statistical analysis of energy confinement for more than 100 H-mode discharges, as shown in Fig. 2, it has been found that the energy confinement improvement factor $H_{98y,2}$ degrades with the density normalized to the Greenwald limit during small-ELM H-mode, type-I ELMy, and type-III ELMy H-mode phases. The type-I and small ELMy regimes exhibit better confinement than that in the type-III ELMy phase, while the repetition frequency of small ELMs (typically >0.8 kHz) is much higher than that in type-III ELMs (typically <0.5 Hz) and type-I ELMs (typically <0.1 kHz).

III. CHARACTERISTICS OF SMALL ELMs

Compared with the type-I and type-III ELMs, one remarkable advantage of the small ELMs is the very small particle and heat transport from the pedestal to divertor target plate. Unfortunately, the pedestal temperature and density are not routinely measured in EAST currently. Instead, it has been found that there is no noticeable decrease in both the plasma stored energy and line-averaged density during the small ELMs, suggesting that they result in low particle and energy losses in the pedestal region. The resulting peak heat load calculated from the divertor Langmuir probe is <1 MW/m^2, which is much smaller than that of type-III ELMs and type-I ELMs.[20] As shown in Fig. 3, the averaged ion saturation currents calculated by conditional averaged of about 100 small ELMs in the outer divertor target plate are less than half of that resulting from the type-III ELMs.

The conventional ELMs, i.e., type-I ELMs and type-III ELMs (Fig. 3(b)), are usually accompanied with non-linear explosion to eject particles and heat and a following slow pedestal recovery phase. These two phases would be responsible for the sharply ($\sim$0.3 ms) increase and long-time (1 ms) decrease in the divertor ion saturation current. This asymmetric shape has also been found in the ion saturation current in both the scrape-off layer (SOL) region and the private flux region. Note that both the probes we choose in the SOL region and private flux region are $\sim$2 cm radially away from
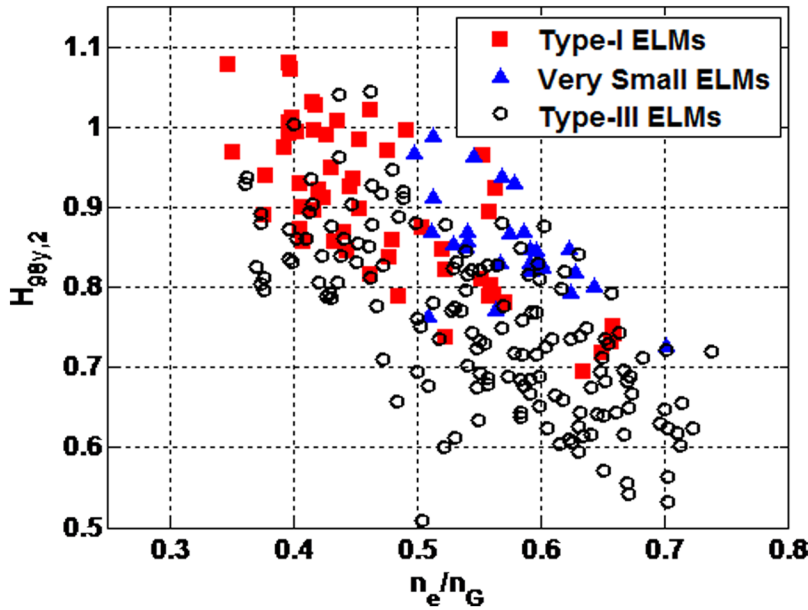
FIG. 2. Confinement factor of type-I (red square), small ELMs (blue triangle), and type-III (black circle) ELMy regimes $H_{98y,2}$ versus normalized density.

the strike point after mapping to the midplane. However, the shape of small ELMs near the strike point appears to be more symmetrical with nearly 0.2 ms increase and 0.3 ms decrease, as shown in Fig. 3(a). The amplitude is much higher than that of SOL region and private flux region. The duration of the small ELMs is ∼1 ms, slightly smaller than that of the type-III ELMs.

ELMs usually result in current filaments moving from inside the separatrix into the SOL region and as detected by the Mirnov coils. The small ELMs also result in magnetic perturbations and have been detected by the Mirnov coils installed behind the first wall. The amplitudes are 5 times smaller than that of the type-III ELMs. In Fig. 4(b), it is

interesting to find that the small ELM induced magnetic oscillations propagate upward in the high-field side and downward in the low-field side, corresponding to the ion and electron diamagnetic drift directions, respectively. This suggests that small ELMs result in a current filament moved in electron diamagnetic drift direction in the low-field side.

IV. DYNAMICS OF THE SMALL ELMs

To date, ELMs are thought to be a class of magnetohydrodynamic modes generated in the pedestal region where the high pressure gradient driven ballooning modes couples to the current density driven peeling modes.[3,21] When the combination of the pressure gradient and current density
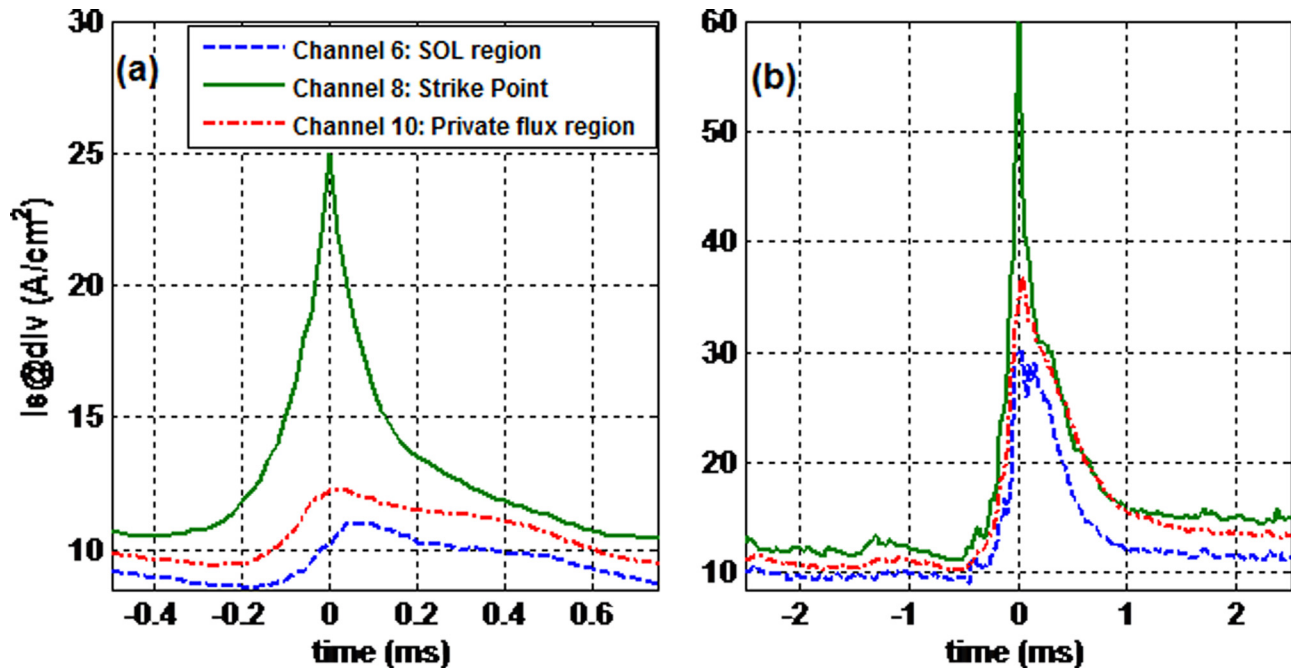

FIG. 3. Shapes of small ELMs (a) and type-III ELMs (b) of ion saturation current in SOL region (blue dashed line), near strike point (green solid line) and private flux region (red dashed-dotted line) calculate by conditional average. Note that both the channel 6 (SOL region) and channel 8 (private flux region) are ∼2 cm radially away from the strike point after mapping to the midplane.
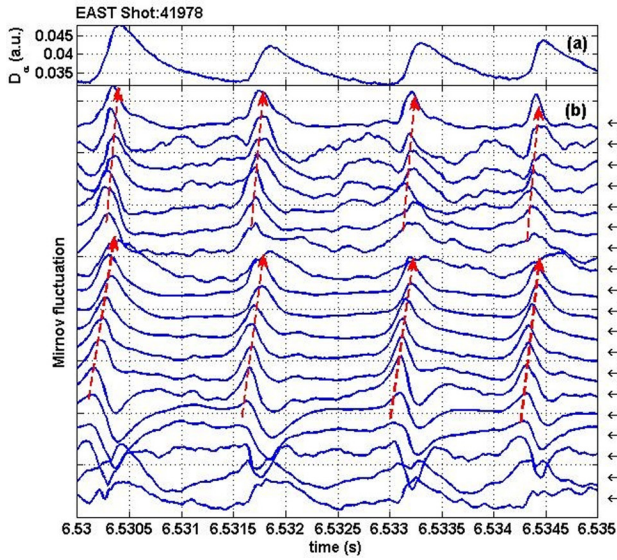
FIG. 4. The small ELM induced magnetic oscillations measured by the Mirnov coils installed behind the first wall. The locations of Mirnov coils are shown in (c). The red-dashed arrow shows the propagating direction. The poloidal location of the fast reciprocating probe is illustrated in (c).

reaches a critical limit, ELMs occur. The type-III ELMs, as the most common ELMs in EAST, have usually been found to accompany coherent electromagnetic precursor oscillation with frequency ranging from 130 kHz to 60 kHz. However, no such precursors have been detected prior to the crashes of the small ELMs. Instead, some electrostatic quasi-coherent oscillations have been observed in the small ELMs, as shown in Fig. 5. Detailed information on the small ELM is provided by 4-tip graphite probe arrays inside but close to the separatrix, installed on the reciprocating probe systems at the outboard midplane.[22] The probe geometry is shown in Fig. 5. Two tips in the middle of the probe are used as a double-probe and the other two tips on each side, poloidally spaced by 7 mm, for floating potential measurements, i.e., ϕ_{f3} and ϕ_{f4}, with each tip of 2 mm in length. This probe array can provide simultaneous measurements of electron density, n_e, electron temperature, $T_e = (\phi_+ - \phi_f)/\ln 2$, and plasma potential, $\phi_p = \phi_f + 2.8 T_e$, where ϕ_+ is the potential measured by the positively biased tip and $\phi_f = (\phi_{f3} + \phi_{f4})/2$. Fluctuation-driven particle and heat flux can be estimated to

be $\Gamma = \delta E_p \delta n_e / B$ and $Q = \frac{3}{2} \Gamma \langle T_e \rangle + \langle n_e \rangle \delta E_p \delta T_e / B$, respectively, where δE_p, δT_e, and δn_e are poloidal electric field fluctuation, temperature fluctuations, and density fluctuations. Here, we calculate the fluctuation by using high-pass (>0.5 kHz) filter and angle brackets represents the ensemble average.

Figure 6 clearly shows that each small ELM corresponds to a cluster of several ($\sim$10) spikes, negative spikes in the floating potential and positive spikes in the ion saturation current. When the small ELMs are asymmetrical between 6.720 s and 6.730 s, the cluster of the spikes in the floating
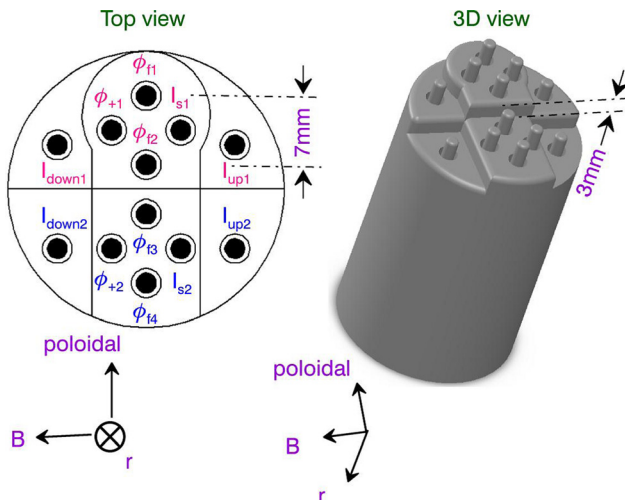

FIG. 5. The probe tip geometry used in the EAST experiment. There are two set of 4-tip probes, while only the ϕ_{f3}, ϕ_{f4}, ϕ_{+2}, and I_{s2} are available and used in the small-ELM phase.
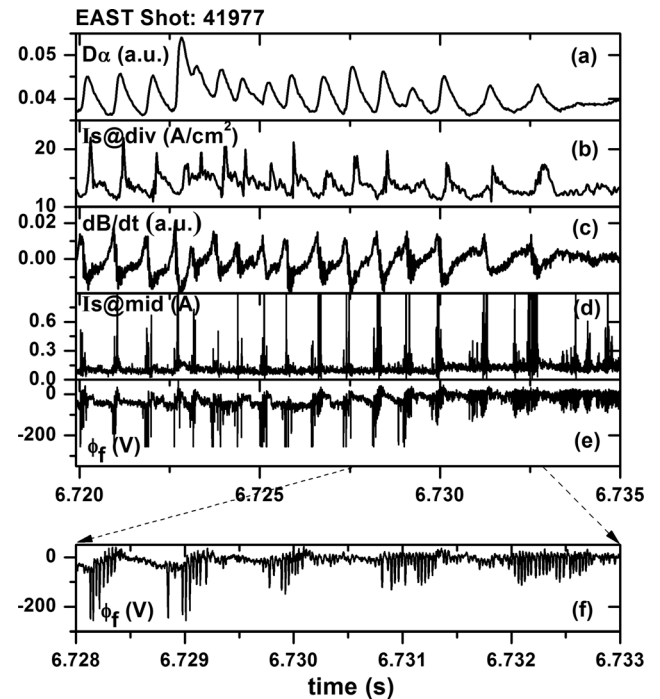

FIG. 6. (a) Divertor D_α emission, (b) divertor ion saturation current measured by Langmuir probe, (c) magnetic perturbation measured by the Mirnov coils installed at the midplane of high-field side, (d) ion saturation current measurement by four-tip probe at midplane installed on fast reciprocating probe, (e) floating potential measured by four-tip probe, (f) zoom-in plot of floating potential in (e).
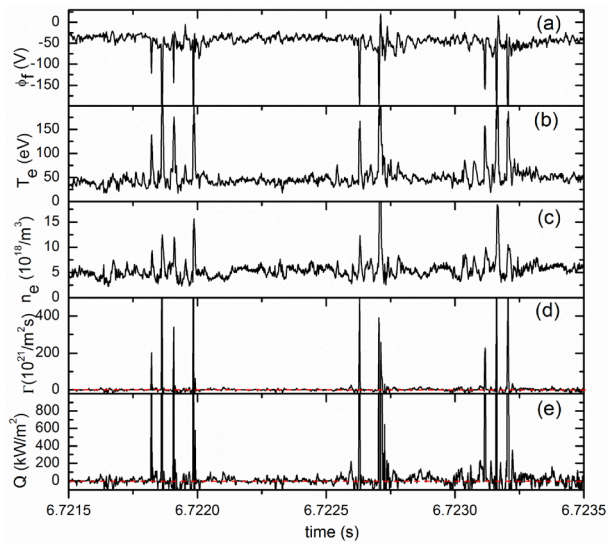
FIG. 7. Time evolution of the edge parameters of small ELMs measured by the fast probe near the separatrix. (a) floating potential, (b) electron temperature, (c) electron density, (d) fluctuation-driven particle flux, and (e) fluctuation-driven heat flux. Here, positive flux means outward transport.

FIG. 9. The XUV radiations of small ELMs with chords toward divertor (blue line) and through the outboard midplane (red line). The red one clearly shows quasi-coherent burst.

potentials appear to be short and sharp, while between 6.730 s and 6.735 s, both the small ELMs and the spike cluster appear to be more symmetrical. These spikes have been also found in the ion saturation current in the SOL near the separatrix, but not found in the far SOL, suggesting the sharp decay in the SOL which agrees with the sharp decay of the small ELMs. The electron temperature and density at the spikes (Fig. 7), measured by the 4-tip probe, are 150 eV and $1.5 \times 10^{19}\,\mathrm{m^{-3}}$, respectively, about 4 times of that between ELMs. Furthermore, there are also spikes in the estimated fluctuation-driven particle and heat fluxes with peak much higher than that between ELMs, indicating that the spiky

structure would drive strong particle and heat transport across the field lines and into the SOL.

The spikes reveal quasi-periodicity with a period around 30 μs in the time domain, by detailed tracking the evolution of the small ELMs. As shown in Fig. 8, detailed correlation analysis between the two 7 mm poloidally separated floating potentials reveals a peak exists at nearly 31 kHz with a strong correlation coefficient ~0.9 and exhibits the second harmonic, which is possibly due to the spike waveform. The FWHM (full width at half maximum) of the quasi-coherent mode is about 12 kHz, which is ~40% of the peak frequency. In addition, from the phase spectrum, the coherent mode propagates in the electron diamagnetic drift direction in the lab frame with the poloidal cross phase about ~0.1π, i.e., the poloidal wavelength $\lambda_\theta \sim 14$ cm, which corresponds to a
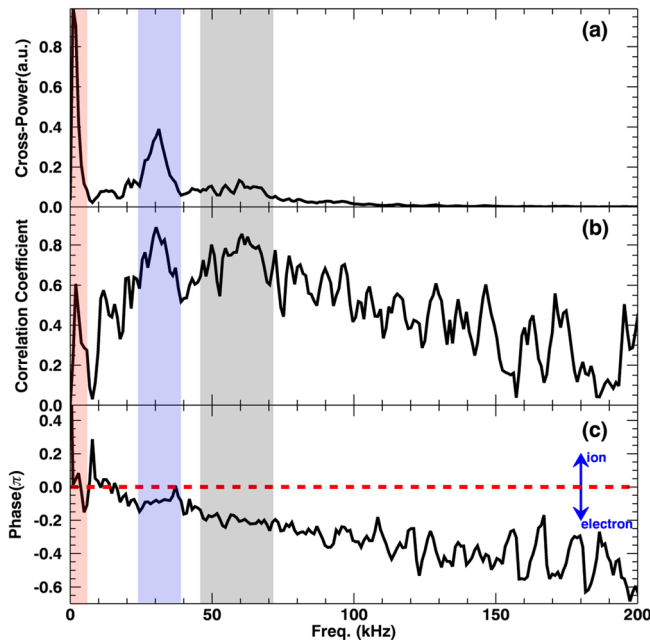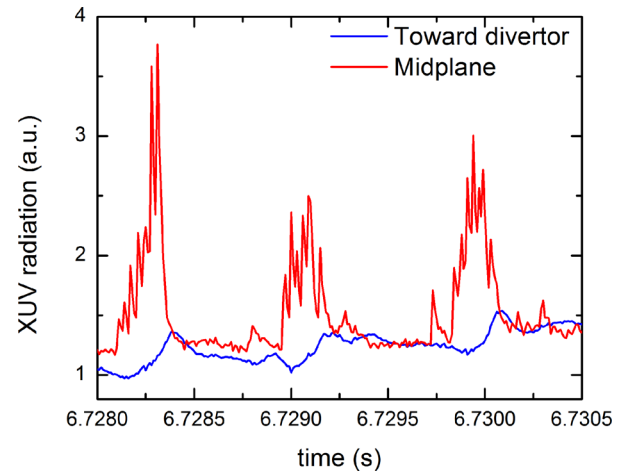

FIG. 8. (a) Normalized cross-power spectrum of two 8 mm poloidally separated floating potential, (b) correlation coefficient spectrum, (c) poloidal phase spectrum.
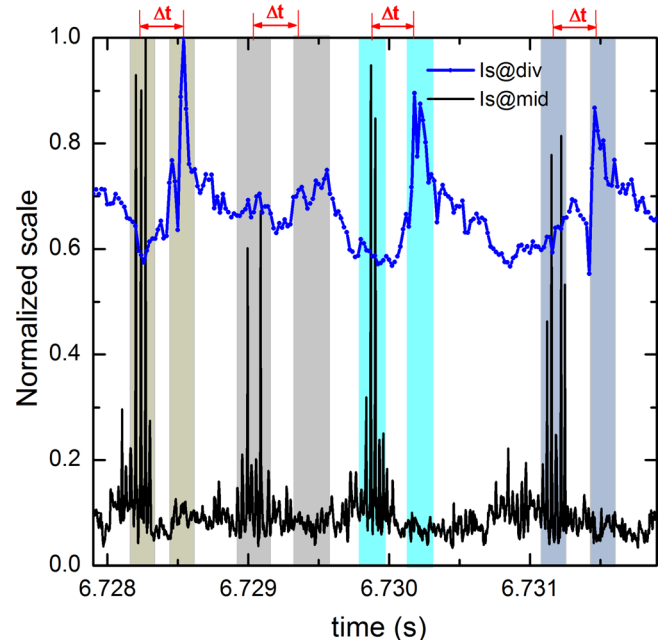

FIG. 10. The time evolution of the ion saturation currents at divertor target plate (red-circle line) and at midplane (black solid line) measured by fast probe at the low-field side midplane.

poloidal mode number m over 60. The toroidal mode number n is estimated to be higher than 12. The associated magnetic perturbations, as detected by small magnetic coils in SOL mounted on a fast reciprocating probe in similar discharges, are much smaller than 1G ($\delta B/B_p \sim 1 \times 10^{-4}$) in the poloidal direction, suggesting the electrostatic nature of the coherent mode. It is noted that the magnetic perturbation can only be detected by the fast Mirnov coils localized at the low-field side when the plasma boundary moves close to the outer wall, but not observed at the high-field side. These coherent spiky oscillations are thought to be another form of the edge coherent modes reported in Ref. 24, with similar frequency, poloidal wavelength, and dispersion relation. The edge coherent mode was considered to play an important role in EAST long-pulse H-modes.

The coherent spiky oscillations in the small ELMs have also been observed in the extreme ultra-violet (XUV) radiation with the chord through the midplane, but not detected toward divertor region. The XUV radiation is measured by a 32-channel bolometer array.[23] In common cases, there are no spiky oscillations in XUV radiation in the small ELMs. In the period, as shown in Fig. 9, the penetrating probes may introduce impurities that interact with the coherent spiky structure and enhance the radiation as detected by the XUV array. These results are consistent with those measured by the Langmuir probe.

The coherent spikes can be found in the ion saturation current, suggesting that they possibly drive significant particle transport. As can be seen in Fig. 10, it is interesting to find that the upstream ion saturation current spikes at the outer-midplane measured by the fast reciprocating probes are strongly correlated with the downstream ion saturation current measured by the Langmuir probes embedded in the divertor plate. The higher spikes at upstream correspond to larger peak at downstream. The time delay is about 300–400 μs, which is close to the estimated parallel transport timescale in the SOL, $\tau = \frac{L_{||}}{c_s} \approx 300 - 400\,\mu$s. Here, $L_{||}$ is the connect length and c_s is ion acoustic speed in SOL, assuming the temperature about 50–150 eV. Note that the lower peaks, i.e., at 6.729 s, have a longer time delay between the upstream and downstream than the higher peaks, i.e., at 6.728 s, possibly arising from a higher temperature at the higher spikes. This suggests that the coherent-mode filament structure enhances strong transport from the pedestal region into the scrape-off layer and towards the divertor plate.

V. CONCLUSIONS

A small ELMy H-mode regime has been achieved in EAST at a relative high collisionality at the pedestal top $\nu_e^* > 1$ with energy confinement enhanced factor $H_{98y,2}$ up to 1 by using the LHCD and ICRF heating and lithium wall conditioning. Small ELMs usually exhibit high repetition frequency and small energy loss. Detailed measurements from the probes clearly show that a quasi-coherent mode co-exists with the small ELMs. The coherent mode, without strong magnetic perturbations in contrast to the conventional ELMs, propagates in the electron diamagnetic drift direction in the lab frame with the poloidal wavelength $\lambda_\theta \sim 14$ cm.

Furthermore, the coherent-mode filament-like structure promotes transport from the pedestal region into the SOL and eventually towards divertor region, which is beneficial for the sustainment of the H-mode regime without the appearance of giant ELMs, similar to the type-II ELMs.[15,24]

However, it is still unclear what causes the strong magnetic perturbation propagating in the electron diamagnetic drift direction. This will be further investigated in the future, and efforts will also be made to extend this small-ELM H-mode operation toward low-collisionality regimes $\nu_e^* < 0.1$, which are relevant to ITER and future reactors.

[1]F. Wagner, G. Becker, K. Behringer, D. Campbell, A. Eberhagen, W. Engelhardt, G. Fussmann, O. Gehre, J. Gernhardt, G. Gierke, G. Haas, M. Huang, F. Karger, M. Keilhacker, O. Klüber, M. Kornherr, K. Lackner, G. Lisitano, G. Lister, H. Mayer, D. Meisel, E. Müller, H. Murmann, H. Niedermeyer, W. Poschenrieder, H. Rapp, H. Röhr, F. Schneider, G. Siller, E. Speth, A. Stäbler, K. Steuer, G. Venus, O. Vollmer, and Z. Yü, Phys. Rev. Lett. **49**, 1408 (1982).

[2]ITER Physics Expert Groups on Confinement and Transport, Confinement Modelling and Database, and ITER Physics Basis Editors, Nucl. Fusion **39**, 2175 (1999).

[3]P. B. Snyder, H. R. Wilson, J. R. Ferron, L. L. Lao, A. W. Leonard, T. H. Osborne, A. D. Turnbull, D. Mossessian, M. Murakami, and X. Q. Xu, Phys. Plasmas **9**, 2037 (2002).

[4]A. Kirk, H. Wilson, G. Counsell, R. Akers, E. Arends, S. Cowley, J. Dowling, B. Lloyd, M. Price, and M. Walsh, Phys. Rev. Lett. **92**, 245002 (2004).

[5]H. Zohm, Plasma Phys. Controlled Fusion **38**, 105 (1996).

[6]J. W. Connor, R. J. Hastie, H. R. Wilson, and R. L. Miller, Phys. Plasmas **5**, 2687 (1998).

[7]G. Federici, A. Loarte, and G. Strohmayer, Plasma Phys. Controlled Fusion **45**, 1523 (2003).

[8]A. Mazurenko, M. Porkolab, D. Mossessian, J. Snipes, X. Xu, and W. Nevins, Phys. Rev. Lett. **89**, 225004 (2002).

[9]K. Burrell, T. Osborne, P. Snyder, W. West, M. Fenstermacher, R. Groebner, P. Gohil, A. Leonard, and W. Solomon, Phys. Rev. Lett. **102**, 155003 (2009).

[10]E. R. Solano, P. J. Lomas, B. Alper, G. S. Xu, Y. Andrew, G. Arnoux, A. Boboc, L. Barrera, P. Belo, M. N. A. Beurskens, M. Brix, K. Crombe, E. de la Luna, S. Devaux, T. Eich, S. Gerasimov, C. Giroud, D. Harting, D. Howell, A. Huber, G. Kocsis, A. Korotkov, A. Lopez-Fraguas, M. F. F. Nave, E. Rachlew, F. Rimini, S. Saarelma, A. Sirinelli, S. D. Pinches, H. Thomsen, L. Zabeo, and D. Zarzoso, Phys. Rev. Lett. **104**, 185003 (2010).

[11]N. Oyama, P. Gohil, L. D Horton, A. E. Hubbard, J. W. Hughes, Y. Kamada, K. Kamiya, A. W. Leonard, A. Loarte, R. Maingi, G. Saibene, R. Sartori, J. K. Stober, W. Suttrop, H. Urano, W. P. West, and ITPA Pedestral Topical Group, Plasma Phys. Controlled Fusion **48**, A171 (2006).

[12]Y. Kamada, T. Oikawa, L. Lao, T. Takizuka, T. Hatae, A. Isayama, J. Manickam, M. Okabayashi, T. Fukuda, and K. Tsuchiya, Plasma Phys. Controlled Fusion **42**, A247 (2000).

[13]R. Maingi, K. Tritz, E. D. Fredrickson, J. E. Menard, S. A. Sabbagh, D. Stutman, M. G. Bell, R. E. Bell, C. E. Bush, D. A. Gates, D. W. Johnson, R. Kaita, S. M. Kaye, H. W. Kugel, B. P. LeBlanc, D. Mueller, R. Raman, A. L. Roquemore, and V. A. Soukhanovskii, Nucl. Fusion **45**, 264 (2005).

[14]T. Ozeki, M. S. Chu, L. L. Lao, T. S. Taylor, M. S. Chance, S. Kinoshita, K. H. Burrell, and R. D. Stambaugh, Nucl. Fusion **30**, 1425 (1990).

[15]E. Wolfrum, M. Bernert, J. E. Boom, A. Burckhart, I. G. J. Classen, G. D. Conway, T. Eich, R. Fischer, A. Gude, A. Herrmann, N. C. Luhmann, M.

Maraschek, R. McDermott, H. K. Park, T. Pütterich, J. Vicente, B. Wieland, and M. Willensdorfer, Plasma Phys. Controlled Fusion **53**, 085026 (2011).

[16]J. E. Boom, E. Wolfrum, I. G. J. Classen, P. C. de Vries, M. Maraschek, W. Suttrop, C. P. P. von Thun, A. J. H. Donné, B. J. Tobias, C. W. Domier, N. C. Luhmann, and H. K. Park, Nucl. Fusion **52**, 114004 (2012).

[17]Y. X. Wan, HT-7 Team, and HT-7U Team, Nucl. Fusion **40**, 1057 (2000).

[18]H. Q. Wang, G. S. Xu, H. Y. Guo, B. N. Wan, V. Naulin, S. Y. Ding, N. Yan, W. Zhang, L. Wang, S. C. Liu, R. Chen, L. M. Shao, H. Xiong, P. Liu, M. Jiang, and G. N. Luo, Nucl. Fusion **52**, 123011 (2012).

[19]B. Wan, J. Li, H. Guo, Y. Liang, and G. Xu, Nucl. Fusion **53**, 104006 (2013).

[20]L. Wang, G. S. Xu, H. Y. Guo, H. Q. Wang, S. C. Liu, K. F. Gan, X. Z. Gong, Y. Liang, N. Yan, L. Chen, J. B. Liu, W. Zhang, R. Chen, L. M. Shao, H. Xiong, J. P. Qian, B. Shen, G. J. Liu, R. Ding, X. J. Zhang, C. M.

Qin, S. Ding, L. Y. Xiang, G. H. Hu, Z. W. Wu, G. N. Luo, J. L. Chen, L. Q. Hu, X. Gao, B. N. Wan, and J. G. Li, Nucl. Fusion **53**, 073028 (2013).

[21]H. R. Wilson, J. W. Connor, A. R. Field, S. J. Fielding, R. L. Miller, L. L. Lao, J. R. Ferron, and A. D. Turnbull, Phys. Plasmas **6**, 1925 (1999).

[22]W. Zhang, J. F. Chang, B. N. Wan, G. S. Xu, C. J. Xiao, B. Li, C. S. Xu, N. Yan, L. Wang, S. C. Liu, M. Jiang, and P. Liu, Rev. Sci. Instrum. **81**, 113501 (2010).

[23]Y. M. Duan, L. Q. Hu, S. T. Mao, P. Xu, K. Y. Chen, S. Y. Lin, G. Q. Zhong, J. Z. Zhang, L. Zhang, and L. Wang, Plasma Sci. Technol. **13**, 546 (2011).

[24]H. Q. Wang, G. S. Xu, B. N. Wan, S. Y. Ding, H. Y. Guo, L. M. Shao, S. C. Liu, X. Q. Xu, E. Wang, N. Yan, V. Naulin, A. H. Nielsen, J. J. Rasmussen, J. Candy, R. Bravenec, Y. W. Sun, T. H. Shi, Y. F. Liang, R. Chen, W. Zhang, L. Wang, L. Chen, N. Zhao, Y. L. Li, Y. L. Liu, G. H. Hu, and X. Z. Gong, Phys. Rev. Lett. **112**, 185004 (2014).